Investigation of the Heat Treatment Regimes on the Structure and Microhardness of Laser Direct Energy Deposition Aluminum Alloy AlSi10Mg

Darya Volosevich *, Zhanna Shabunina, Nikita Yurchenko, Ruslan Mendagaliev, Edem Slatenko, Georgii Klimov, Olga Klimova-Korsmik [ID] and Aleksey Eremeev

World-Class Research Center "Advanced Digital Technologies", State Marine Technical University, Saint Petersburg 190121, Russia; shabunina@ilwt.smtu.ru (Z.S.); yurchenko@ilwt.smtu.ru (N.Y.); mendagaliev@smtu.ru (R.M.); slatenko@ilwt.smtu.ru (E.S.); klimovgg@gmail.com (G.K.); o.klimova@ltc.ru (O.K.-K.); eadst@yandex.ru (A.E.)
* Correspondence: d.volosevich@ilwt.smtu.ru

Abstract: This study investigates the influence of various heat treatment regimes on the structure and microhardness of the aluminum alloy AlSi10Mg processed by the L-DED method. The study considers heat treatment regimes for solid solution in the temperature range of $500-540\ ^\circ$C with holding times of 30–120 min, as well as artificial aging regimes in the temperature range of $160-190\ ^\circ$C with holding times of 4–8 h. As a result of studying the structure and mechanical properties of the heat-treated samples, it became clear that the optimal regime can be considered the regime of $500\ ^\circ$C for 30 min followed by $190\ ^\circ$C for 6 h. This regime leads to the formation of a uniform structure with the breakage of the eutectic network into separate spherical silicon inclusions. The microhardness in this case is 90 HV, which is 55% higher than the initial state. Using TEM, it was established that the reason for the increase in hardness is the formation of nanoscale inclusions β'' (Mg_5Si_6).

Keywords: aluminum alloy; AlSi10Mg; L-DED; heat treatment; solution annealing; artificial aging

1. Introduction

It is known that additive manufacturing has a number of undeniable advantages over traditional technologies [1–3] and therefore attracts significant attention from researchers around the world [4–6]. A special place among additive technologies is occupied by laser additive manufacturing (LAM), for example, laser direct energy deposition (L-DED), which uses powder as the raw material, melted using laser radiation. The use of a concentrated laser beam as a heat source, on the one hand, contributes to some reduction in productivity, and the use of powder as the raw material leads to a decrease in the material utilization factor (compared, for example, with wire arc additive technologies). On the other hand, this technology is ideally suited for the production of medium-sized products, for which high growth accuracy and low roughness are required, and moreover, L-DED is characterized by reduced heat input into the material and the formation of the most uniform structures as a result.

Among the most common materials (steels, titanium, and nickel alloys) [7–9], LAM of non-ferrous metals presents a special challenge due to their high reflectivity. Despite this, there are a wide range of studies devoted to selective laser melting (SLM) production from aluminum alloys [10–13], while L-DED from aluminum alloys [14–16] attracts significantly less attention.

Aluminum alloys are characterized by low weight, high specific strength, and corrosion resistance, and are therefore actively used in aviation, rocket-, and shipbuilding. Aluminum alloy AlSi10Mg is a heat-treatable alloy, and therefore, heat treatment regimes are well known for casting. It is known that the fundamental differences in the processes of casting and SLM lead to the formation of completely different structures and different mechanical behavior, as shown, for example, in studies [17,18]. According to the research results, due to the differences in the casting and SLM processes, the structure of the cast alloy is represented by a solid solution of Si and Mg in α-Al, coarse eutectic, as well as large Mg-rich inclusions. At the same time, the structure of the SLM alloy is represented by finer α-Al cells surrounded by a network of Si, which consists of individual Si plates, as well as significantly smaller second-phase inclusions. Such significant differences in the microstructure of alloys for different manufacturing processes have led researchers to the need to select new heat treatment regimes [17–20]. These studies report that traditional T6 heat treatment is preferable for cast Al-Si-Mg alloys, as it promotes the homogenization of the coarse cast structure and improves the mechanical properties of the alloy. However, it is also reported that the high temperatures characteristic of the first stage of T6 promote the breakage of the fine eutectic Si network and significant coarsening of spherical particles, leading to a serious decrease in strength and hardness, which are not restored even in subsequent stages of heat treatment [17,18]. Therefore, many researchers have concluded that for the SLM process, the most preferable heat treatment is DA, T4 [17], or at least requires a reduction in the solution treatment temperature [18]. As a result of numerous studies, the degree of development of heat treatment of the SLM AlSi10Mg alloy is sufficient, and mechanisms are known that allow full control of the structure and mechanical properties depending on the heat treatment parameters.

It is also reasonable to assume that the structures for SLM and L-DED processes also have their differences. SLM technology is characterized by the formation of fine weld beads, which leads to differences in the temperature gradient arising in the melt pool [17,18]. There are only a small number of studies on L-DED from the AlSi10Mg alloy, but it is already clear from them that due to the different thermal history within the weld bead, structures are formed that differ in the size of α-Al cells, the morphology of the eutectic Si network, grain size, as well as the size of phase constituents [15–18]. The main difference that can affect the choice of heat treatment regimes is the morphology of the eutectic Si network. As can be seen from the results [17,18], the morphology of the eutectic Si network consists of thin individual plates surrounding the cells of the α-Al solid solution, while from the studies [15,16], it is clear that in L-DED, Si is precipitated along the boundaries of α-Al cells already in the form of a developed network of parallel thin plates. In this case, the temperature and holding time during heat treatment should ensure the most complete dissolution of the phases, which naturally depends on the morphology and size of the phases under consideration. Thus, the authors of the study suppose that the direct transfer of existing heat treatment regimes to L-DED samples is not correct, and there is a need to consider different heat treatment regimes for the L-DED process, but to the authors' knowledge, such studies do not exist.

This study will investigate the influence of heat treatment regimes, solution annealing, and artificial aging on the structure and microhardness of the aluminum alloy AlSi10Mg obtained by the L-DED method.

2. Materials and Methods

2.1. Materials

AlSi10Mg powder (RUSAL, Moscow, Russia) was used as the raw material for the production of samples. Figure 1 shows images of the particle surfaces, and Table 1 shows the results of the EDS analysis of the particle cross-section.
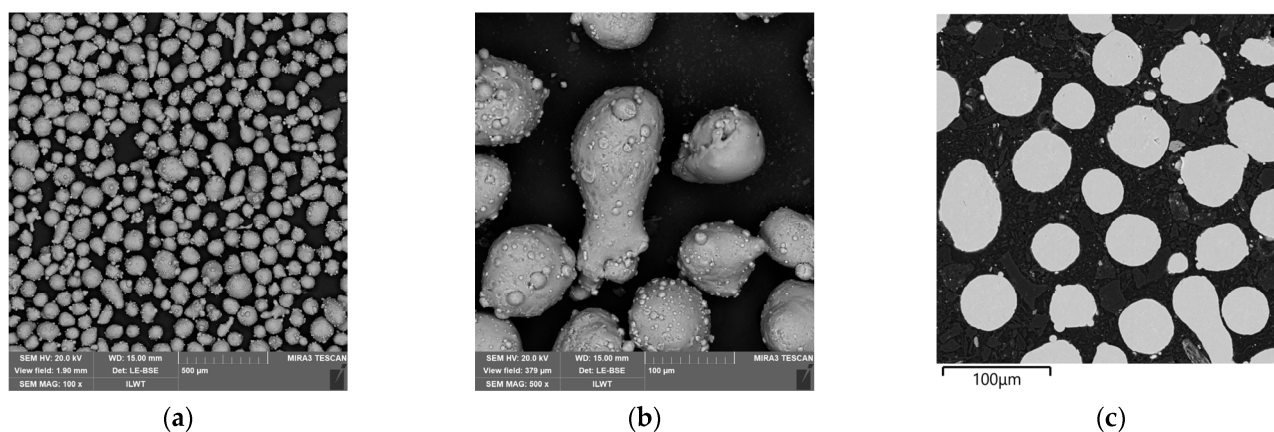

Figure 1. BSE images of the powder ((**a**) powder surface at low magnification; (**b**) powder surface at high magnification; (**c**) powder cross-section).

Table 1. Results of EDS analysis of the particle cross-section (wt.%).

Chemical Element	Mg	Si	Al	Fe
Value	0.32	10.52	89.11	0.05
Standard deviation	0.05	0.57	0.59	0.02

The sizes of the powder particles, as well as their shape, were determined using ImageJ software V.1.53e in accordance with GOST 23402-78 [21] and GOST 25849-83 [22]. The data are presented based on the analysis of at least 500 particles. The powder fraction is 25–150 μm, with d_{10} = 53 μm, d_{50} = 78 μm, and d_{90} = 107 μm. Overall, 47% of the particles have a spherical shape, 52% have a rounded shape, and 1% have an ellipsoidal shape.

2.2. L-DED

The samples were grown using the ILIST-M L-DED setup (ILWT, Saint Petersburg, Russia) with a fiber laser. The L-DED parameters were as follows: power—2000 W; speed—20 mm/s; gas flow rate—3 L/min; width offset—1.33 mm; height offset—0.6 mm; spot diameter—1.8 mm; powder feeding rate—2.5 g/min; pause—40 s. The scanning strategy is shown in Figure 2a. The selection of parameters for L-DED was based on previous experiments, as presented, for example, in [20]. From previous experiments, it is clear that the key parameters affecting the quality of samples in L-DED are laser power, scanning speed, and gas flow rate. A laser power of 2000 W and a scanning speed of 20 mm/s are preferable for aluminum alloys, as these parameters lead to complete melting of the cladded beads and do not cause overheating of the product and the formation of various deposition defects (such as cracking, coarse structure, etc.). Furthermore, it was found that the gas flow rate has a significant impact on the formation of porosity, with minimum porosity values obtained at a protective gas flow rate of about 3 L/min. The width and height offset, the spot diameter, the powder feeding rate, as well as the pause between layers are parameters that mainly affect the proper formation of the geometry of the cladded beads. Therefore, these parameters were chosen to achieve the desired sample dimensions.
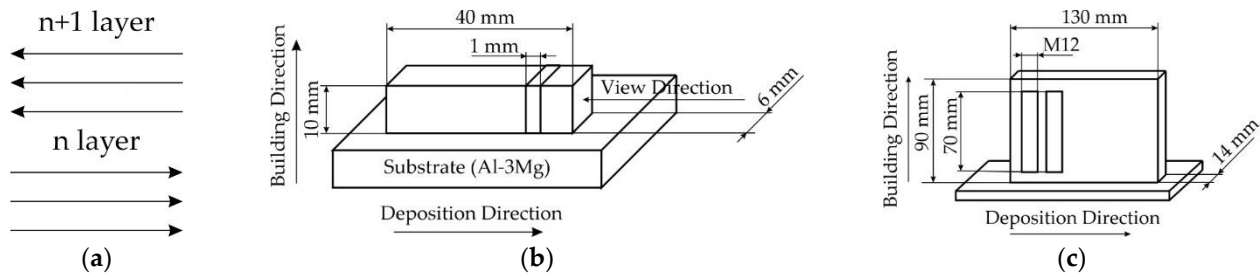
Figure 2. L-DED of the sample ((**a**) scanning strategy; (**b**) structural and phase analysis and micro-hardness measurement; (**c**) mechanical testing).

For structural and phase analysis and microhardness measurement, bars with dimensions of 40 mm × 10 mm × 6 mm were deposited, as shown in Figure 2a. For each heat treatment mode, a plate with a thickness of about 1 mm was cut from such a bar. The structure and microhardness were studied in the direction perpendicular to the deposition direction. For mechanical testing, a plate with dimensions of 130 mm × 90 mm × 14 mm was deposited, and then two M12 cylinders were cut from this plate in the build direction, as shown in Figure 2b. A rolled sample of Al-3Mg alloy was used as the substrate.

2.3. Heat Treatment

For the heat treatment of the samples, an SNOL 40/1200 laboratory resistance furnace (SNOL, Narkunai, Lithuania) was used. The experimental scheme is shown in Figure 3. The selection of the solution treatment regimes was made based on the requirement that the temperature and holding time should ensure the most complete breakage of the eutectic network, while avoiding the negative effects of prolonged high-temperature treatment (grain growth, coarsening of Si inclusions, and reduction of mechanical properties). Thus, a safe and least energy-intensive range was chosen—500–540 °C for 30–120 min, which corresponds to [17–20,23]. It is known that the higher properties after aging can be ensured by prolonged heat treatment at lowered temperatures. On the other hand, in production conditions, long holding times typically do not meet the requirements of economic feasibility. Therefore, the range of 160–190 °C for 4–8 h was chosen, and based on previous experiments [17–20,23], it is expected that within this range, the shortest regime ensuring maximum microhardness can be selected. In the case of solution annealing, the samples were cooled in water at room temperature, and in the case of aging, they were cooled in air. Air cooling provides a moderate cooling rate, which is important for completing diffusion processes and stabilizing the microstructure. Too rapid cooling can 'freeze' unstable intermediate phases, leading to incomplete strengthening or the formation of undesirable phases. To exclude the influence of different cooling rates on the structure and properties of the alloy, all samples after aging were cooled at the same ambient temperature (22 °C), and they were placed on a refractory brick. To protect the samples from natural aging, the samples were immediately loaded into a furnace for artificial aging after solution annealing.
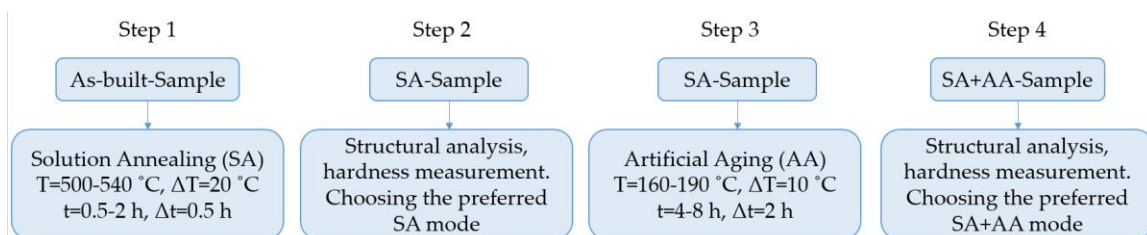

Figure 3. Experimental scheme.

2.4. Structural and Phase Analysis

To study the macrostructure of the samples, an inverted optical microscope Leica DMi8 (Leica Microsystems, Wetzlar, Germany) was used. Energy-dispersive X-ray (EDS) and electron backscatter diffraction (EBSD) analyses were performed using a TESCAN Mira 3 scanning electron microscope (Tescan, Brno-Kohoutovice, Czech Republic) with the appropriate attachments. The step size for EBSD analysis was 1 μm. To study the fine structure, a ThermoFisher Talos transmission electron microscope (TEM) (Thermo Fisher Scientific, Waltham, MA, USA)was used.

To reveal the molten pool boundary (MPB) and eutectic Si networks, the samples were etched in a reagent of 50 mL of H_2O, 2 mL of HNO_3, and 1 mL of HF for 10 s. Foils for TEM study were prepared in a reagent of 730 mL of C_3H_5OH, 100 mL of $C_4H_{10}O_2$, 78 mL of $HClO_4$, and 90 mL of distilled water. For electrolytic etching of the foils, an automatic double-jet electropolishing unit TJ100-SE (Zhengzhou Chuangda Laboratory Equipment Co., Ltd., Zhengzhou, China) was used; the foils were polished at a temperature of −32 °C with an applied voltage of 17 V.

The relative porosity of the sample, the size of α-Al cells, the grain size, and the area of Si inclusions were calculated using ImageJ software. The average α-Al cell size in each of the zones across the cladded bead section was calculated based on at least 30 measurements. The average grain size in each of the zones across the cladded bead was calculated based on at least 50 measurements. The area of spherical Si inclusions was calculated based on at least 100 measurements. Structural analysis as well as microhardness measurements were performed in the cross-section of the samples as shown in Figure 2b.

To exclude the influence of uneven heating of the sample from the bottom layer to the top layer, the structure analysis and microhardness measurement were conducted in the central part of the cross-section of the samples, as shown in Figure 4.
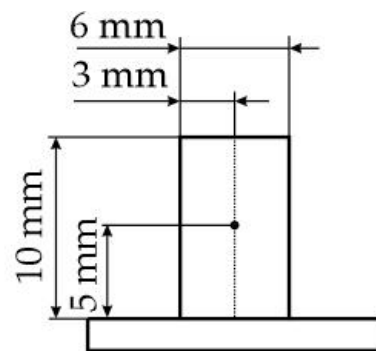

Figure 4. Structural analysis and microhardness measurement scheme.

2.5. Mechanical Testing

The microhardness of the samples was measured using the Vickers method with a Future Tech FM-31 microhardness tester (Future Tech Corp, Kawasaki, Japan). During the microhardness measurement, a distance equal to 300 μm was maintained between the indentations. Measurements were conducted under a load of 10 g, with a holding time of 10 s. Tensile tests were conducted using a Shimadzu AGS-X universal testing machine (Shimadzu, Kioto, Japan) at room temperature in accordance with GOST 1497-2023 [24].

3. Results and Discussion

3.1. As-Built Sample

Figure 5 shows the macrostructure of the deposited sample. As can be seen from the figure, the sample has distinct cladded bead boundaries characteristic of L-DED, with an

average cladded bead height of 0.54 mm and a width of 1.6 mm. Moreover, the sample contains pores. The relative porosity of the sample is 0.8%. The average pore size was 25 µm, with $d_{10} = 9$ µm, $d_{50} = 19$ µm, and $d_{90} = 47$ µm.
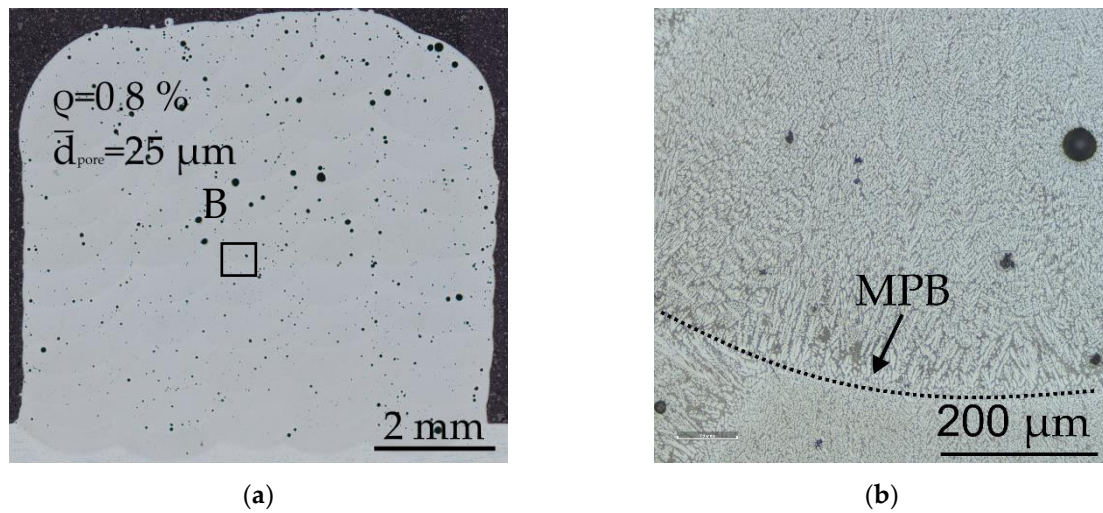

(a)

(b)

Figure 5. Macrostructure of the additively manufactured sample ((**a**) macrostructure at ×2.5 magnification; (**b**) macrostructure at ×10 magnification, enlarged image of section B).

For a more detailed study of the structural features, Figure 6 shows the elemental distribution maps in the cross-section of the sample.
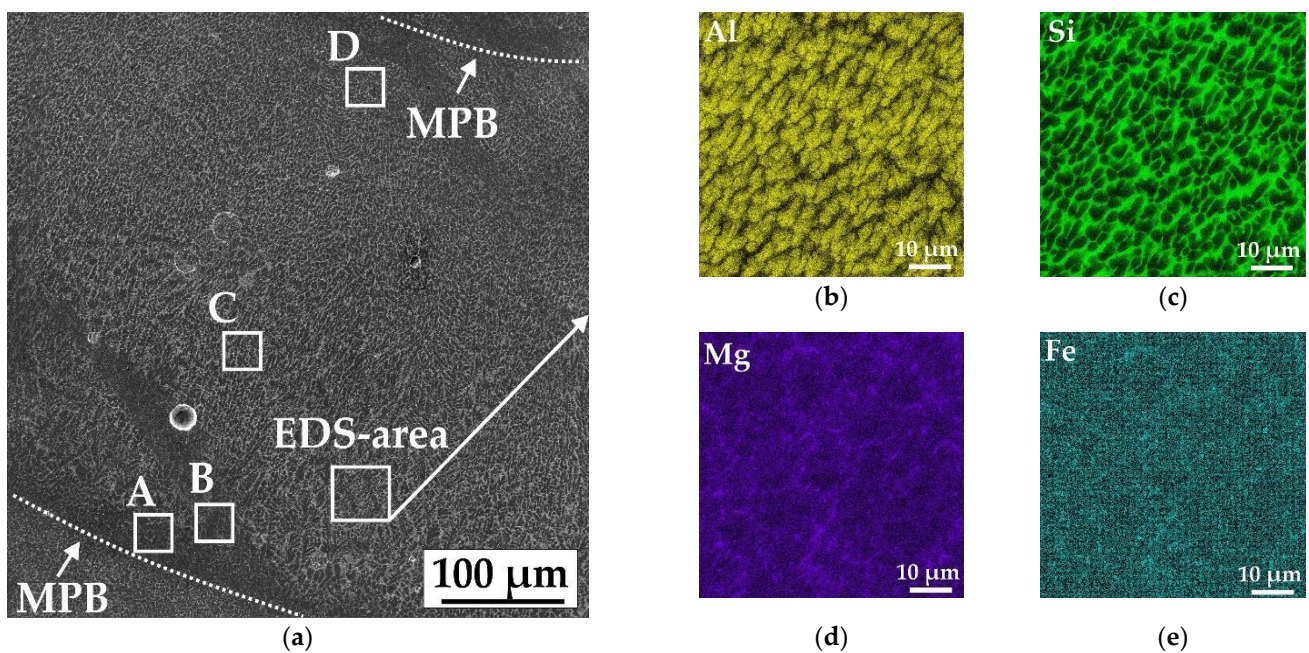

(a)

(b)

(c)

(d)

(e)

Figure 6. Results of EDS analysis of the as-built sample ((**a**) BSE image of the sample cross-section; (**b**) Al distribution map; (**c**) Si distribution map; (**d**) Mg distribution map; (**e**) Fe distribution map).

Figure 7 shows enlarged images of areas A, B, C, and D marked in Figure 6a. From Figure 7, it can be seen that the structure of the aluminum alloy AlSi10Mg is a typical eutectic-type structure and is represented by α-Al cells surrounded by a eutectic Si network. The morphology of Si is a developed network of plates. It is also noted that the morphology of the α-Al cells is non-uniform and changes from the beginning of the cladded bead to its top.
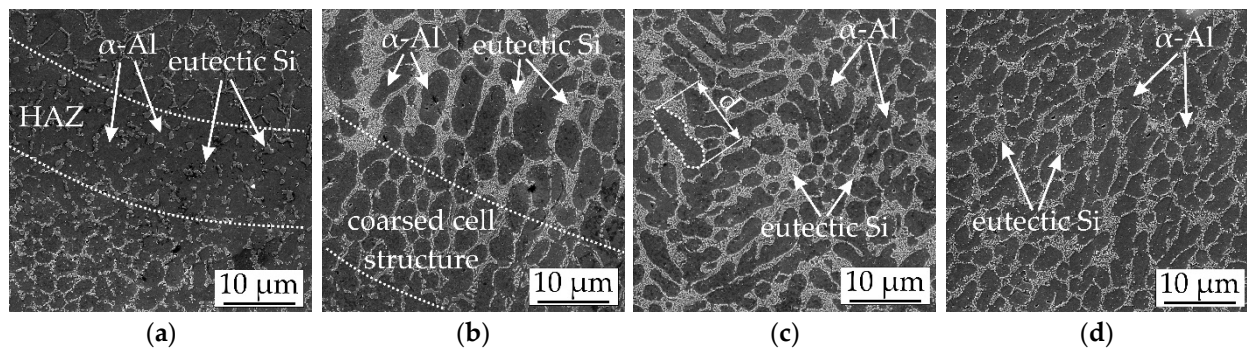
Figure 7. BSE images of the as-built sample ((**a**) HAZ; (**b**) coarse-cell zone; (**c**) dendritic zone; (**d**) fine-cell zone).

In the cross-section of the sample in a single cladded bead, four zones can be distinguished, each characterized by its own size and shape of α-Al cells. The heat-affected zone (HAZ) was determined based on the degree of spheroidization of Si particles [25]. In this work, it was assumed that the HAZ consists of individual spherical or nearly spherical Si particles without the formation of a closed network composed of Si plates. The HAZ demonstrates partial breakage and spheroidization of Si particles, which is associated with repeated cyclic heating and cooling and the formation of quenched structures as a result. Following the HAZ is a zone of large, nearly equiaxed cells with a size of d = 6 μm. The special heat dissipation conditions that arise during L-DED lead to the formation of a directional structure, so in the central part of the cladded bead, a zone of elongated dendrites is observed, predominantly oriented towards the center of the cladded bead, with the size of α-Al cells in this zone being d = 15 μm. Towards the top of the cladded bead, a fine equiaxed cell shape with a size of d = 4 μm is formed.

An Important characteristic of the structure of materials that affects mechanical properties is the grain size, orientation, and shape. Generally, metals and alloys with fine grains have higher mechanical properties: strength, plasticity, toughness, and hardness [26–28]. Conversely, a large grain size leads to poor mechanical properties. To study these factors, EBSD analysis was performed, the results of which are shown in Figure 8. The EBSD analysis revealed a non-uniform grain structure across the cladded bead section: the grains at the MPB have a fine equiaxed shape, followed by a zone of large, nearly equiaxed grains, and towards the end of the cladded bead, large columnar grains oriented predominantly towards the center of the cladded bead are formed. The average grain size at the top of the cladded beads was 60 μm (Figure 8b), that at the cladded bead boundaries was 15 μm (Figure 8c), and that at the bottom of the cladded beads was 74 μm (Figure 8d).

Further mechanical tests for tensile strength and Vickers hardness were conducted. The hardness in the initial state is 58 HV. Figure 9 shows an example of the tensile curve of the same samples in the initial state. The mechanical properties in the initial state are presented in Table 2.
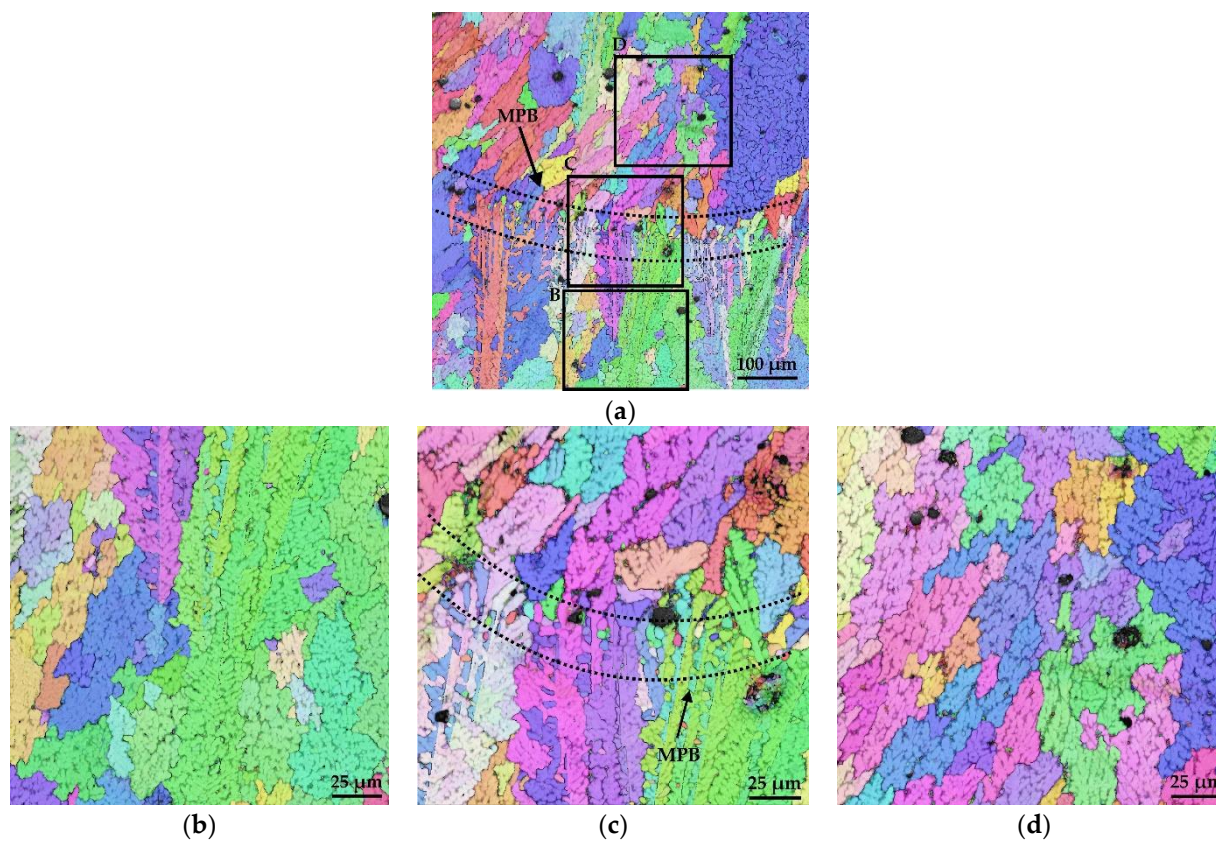
(a)

(b)

(c)

(d)

Figure 8. EBSD analysis results ((**a**) overall image; (**b**) enlarged image of section B; (**c**) enlarged image of section C; (**d**) enlarged image of section D).
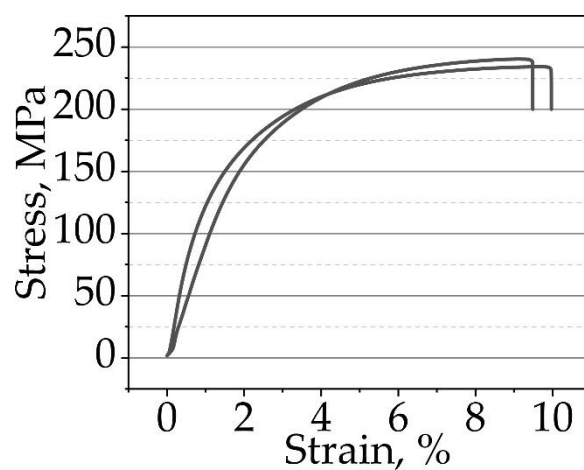

Figure 9. Example of the tensile curve of the samples in the initial state.

Table 2. Mechanical properties of the sample in the initial state.

Parameter	Value
Yield strength σ_{YS}, MPa	140 ± 9
Ultimate strength σ_{UTS}, Mpa	237 ± 4
Elongation δ, %	7.9 ± 0.9

Figure 10 shows the fracture of the sample after tensile testing.
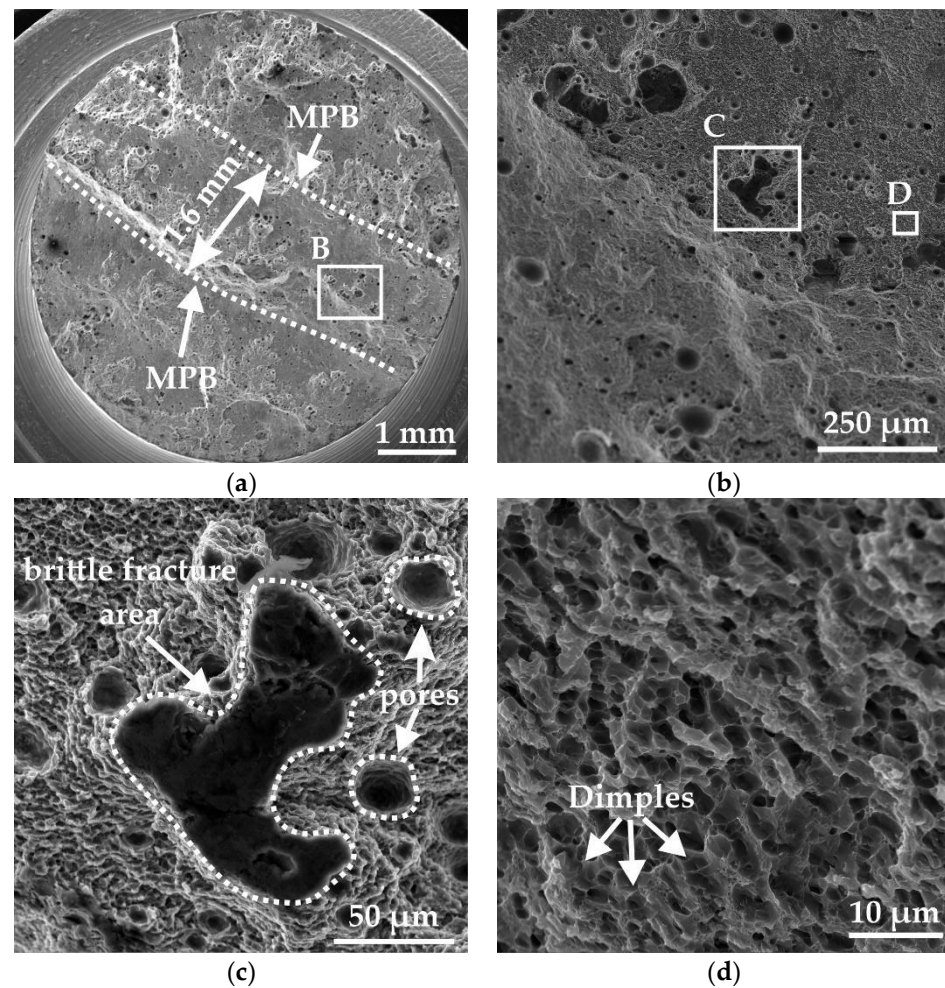
Figure 10. SE image of the fracture ((**a**) overall image; (**b**) enlarged image of section B; (**c**) enlarged image of section C; (**d**) enlarged image of section D).

From Figure 10a, it is evident that the fracture has a fish-scale relief, which is typical for additive manufacturing [29]. The distance between the highest points of the fracture being 1.6 mm, which matches the width of the cladded beads, as shown earlier in Figure 5. Based on this, it is concluded that the failure occurs along the layered structure of the material. With further magnification, it is evident that the fracture predominantly has a dimpled structure, indicating a predominance of ductile failure. The dimples have an almost equiaxed shape, with a size of 3–5 μm. However, flat areas characteristic of brittle failure were also found in the fracture. Such areas are observed only at the MPB, indicating that the likely cause of brittle failure is the localization of pores and coarsening of the eutectic Si phase. Figure 11 shows the fracture of the sample in the section.

As reported earlier, the sample contains pores. In Figure 11b,c, it can be seen that the main stress concentrator during failure is the pores, from which primary macrocracks appear. For the structure "pores + eutectic Si network + α-Al cells," the most likely failure mechanism is as follows: the initiation of primary macrocracks near pores, propagation of the crack along the weakest path—the α-Al-Si boundary—and crack arrest in the most ductile component of the alloy—the α-Al cells. In the absence of pores, the mechanical behavior during deformation is determined by the morphology of the cellular structure of α-Al and the eutectic Si network. As reported in the study [18], in the initial stage of deformation, plastic deformation originates in the soft α-Al matrix, and during the movement of dislocations in the cells, they encounter almost no barrier to movement. The next significant barrier to dislocation movement is likely the coarse eutectic Si network

consisting of thin, elongated plates. Figure 10c shows an image of the eutectic structure after deformation near the failure. Indeed, near the failure, large microvoids are observed forming at the soft matrix–hard Si inclusion boundary. Figure 11d shows an image of the eutectic structure in the cladded bead preceding the failed one, where a decrease in microvoids forming at the α-Al-Si boundary is observed. Apparently, such a cellular structure with a pronounced eutectic Si network leads to difficult deformation transfer and its pronounced localization to the extent that the subsequent layers practically do not change and do not participate in the failure process. On the one hand, such morphology of the eutectic network has a behavior similar to a composite material and can increase the stiffness of the structure and the strength properties of the material. On the other hand, such a pronounced coarse barrier for dislocations can lead to a deterioration of mechanical properties and premature failure of the structure. Therefore, bringing the Si inclusions into a more uniform distribution should have a beneficial effect on the mechanical properties of the material.
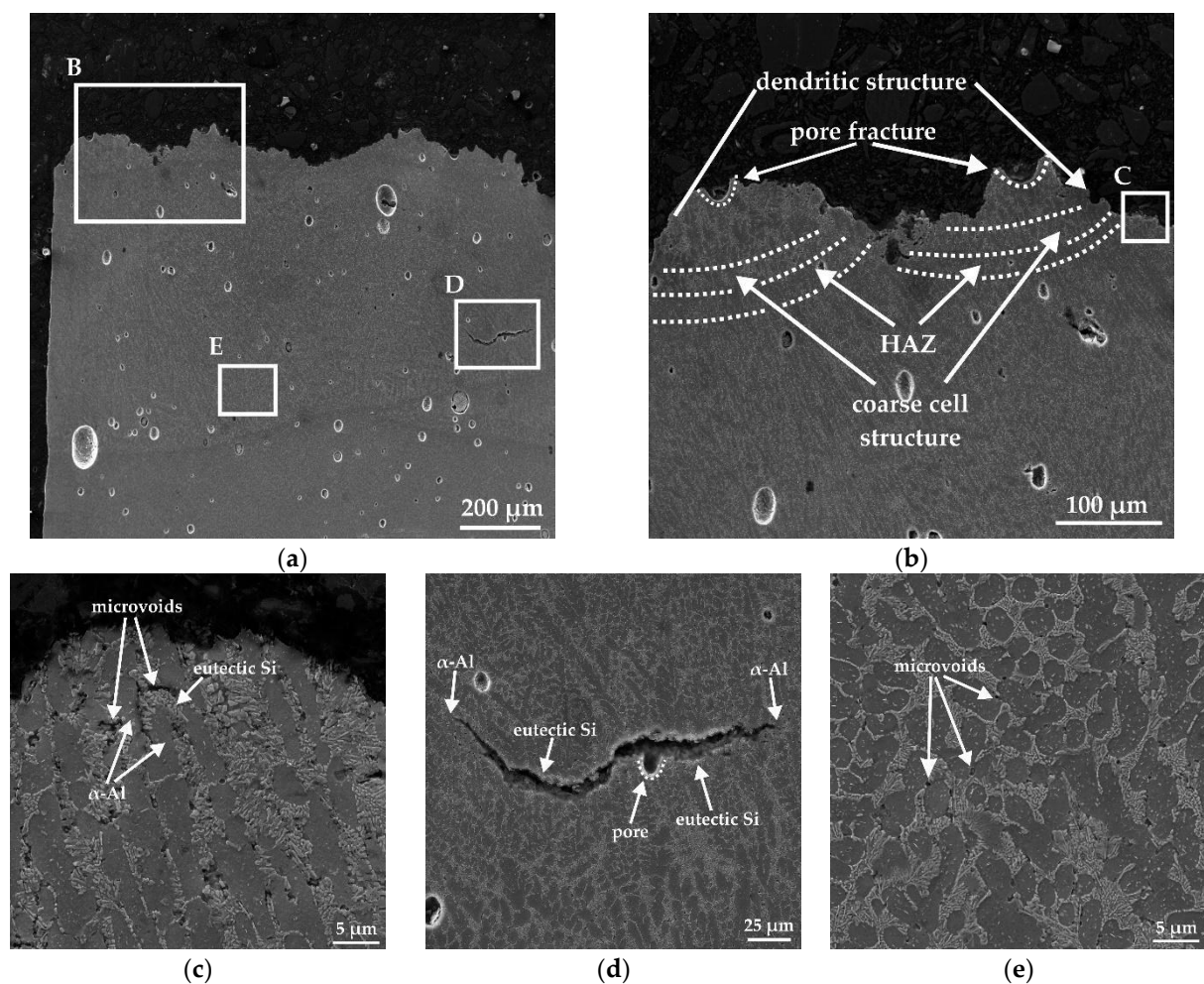

Figure 11. Fracture of the sample in the section after tensile testing ((**a**) overall image; (**b**) enlarged image of section B; (**c**) enlarged image of section C; (**d**) enlarged image of section D; (**e**) enlarged image of section D).

3.2. Solution Annealing

Figure 12 shows the macrostructures of the samples in the annealed states.

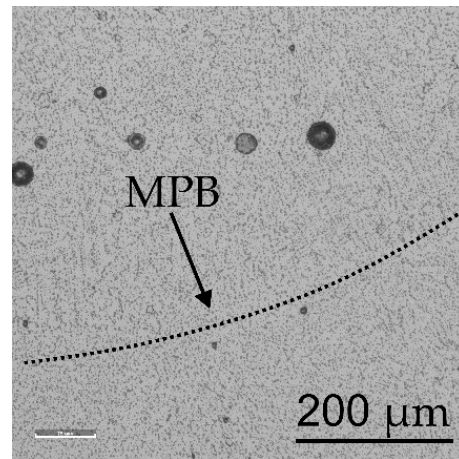**Figure 12.** Macrostructure of the SA sample at ×10 magnification (500 °C, 30 min).

As mentioned earlier, the initial structure of the samples after L-DED has distinct cladded bead boundaries, while the samples after each SA regimes demonstrate a more uniform structure, with no "fish scale" relief observed. Additionally, the uniformity of the structure was assessed using SEM, with the results shown in Figure 13.
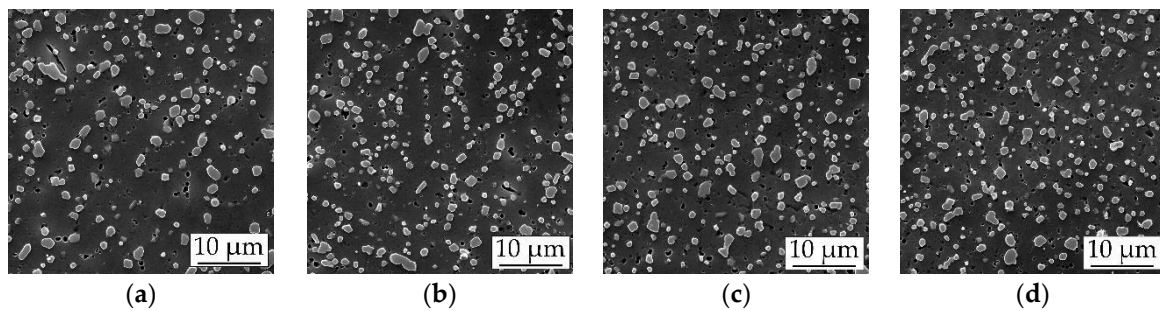

(**a**)   (**b**)   (**c**)   (**d**)

Figure 13. BSE images of the SA sample at 500 °C for 30 min ((**a**) HAZ; (**b**) coarse-cell zone; (**c**) dendritic zone; (**d**) fine-cell zone).

Comparing different zones in the as-built sample with the zones in the SA sample, it can be seen that such heat treatment temperatures lead to the breakage of the eutectic network and partial spheroidization of Si particles, as it was shown in [19]. The morphology of silicon is no longer a developed network of plates but separate spherical inclusions, and the size of these inclusions increases with increasing temperature and holding time. The results of measuring the area of silicon inclusions are shown in Figure 14a and also in Table 3. The minimum inclusion area was obtained for the 500 °C, 30 min regime and is 0.7 μm^2. With an increase in the SA temperature to 540 °C, the inclusion area doubles and is already 1.4 μm^2. With a further increase in holding time, the effect of temperature on the inclusion area weakens noticeably, and for 120 min, the area is 2.1 μm^2 for 500 and 520 °C and 2.3 μm^2 for 540 °C. The likely mechanism for the growth of inclusions is Ostwald ripening, where the growth of larger particles occurs at the expense of the attachment of smaller ones. Significant coarsening of inclusions will inevitably lead to a disruption of cohesion between α-Al cells and Si particles, deteriorate mechanical properties, and therefore, the effect of particle deposition should be minimized by selecting the correct temperatures and holding times.
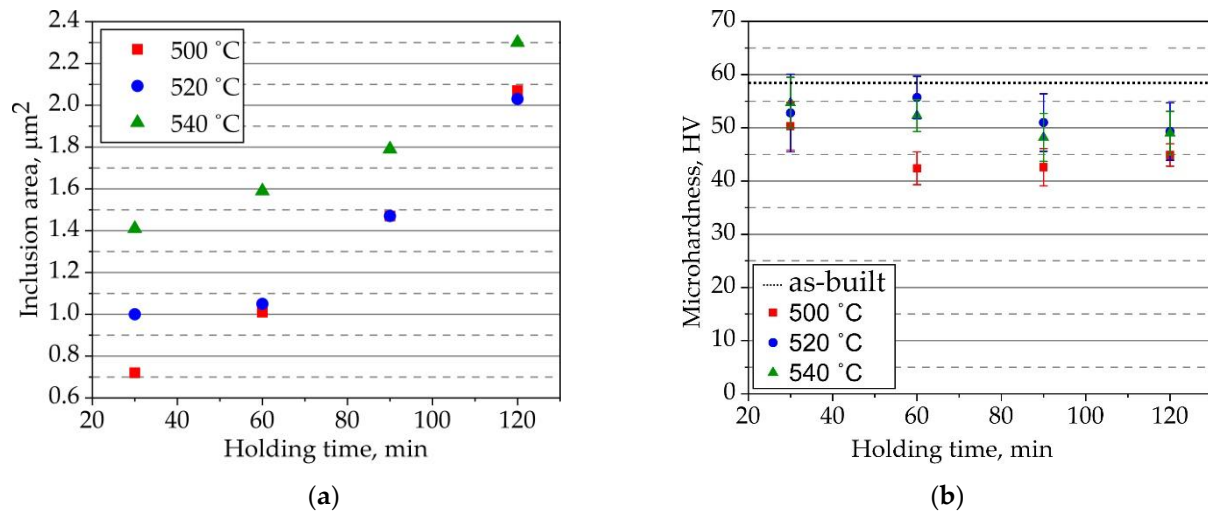
(a)

(b)

Figure 14. Results of measurements ((**a**) particle area; (**b**) microhardness).

Table 3. Results of inclusion area measurement (μm^2).

	500 °C	520 °C	540 °C
30 min	0.71 ± 0.12	1.00 ± 0.16	1.41 ± 0.12
60 min	1.02 ± 0.20	1.06 ± 0.14	1.60 ± 0.15
90 min	1.49 ± 0.17	1.49 ± 0.10	1.80 ± 0.13
120 min	2.08 ± 0.21	2.02 ± 0.21	2.30 ± 0.19

Moreover, it is known [18] that such high treatment temperatures can lead to a significant decrease in hardness, which is not restored even in subsequent aging stages. Therefore, the next criterion for selecting the SA regime is microhardness, the measurement results of which are shown in Figure 14b. Analysis of the graph shows that there is indeed some slight decrease in hardness, but all obtained values are at the level of initial properties. The likely cause of such behavior is a decrease in the proportion of the harder Si network in the material and an increase in the probability of the indentation falling into the softer matrix.

Additionally, to control the quality of SA, EBSD analysis of the samples was performed, the results of which are shown in Figure 15. It was found that both the initial and annealed samples consist of large columnar grains, with small grains at the cladded bead boundaries. Based on the EBSD results, it can be concluded that the 500 °C, 30 min annealing regime did not lead to an increase in grain size, and the average grain size at the top of the cladded beads was 62 μm (Figure 15b), that at the cladded bead boundaries was 15 μm (Figure 15c), and that at the bottom of the cladded beads was 85 μm (Figure 15d).

From the results of studying the SA samples, it is evident that all the studied regimes allow achieving the goal of SA and lead to the formation of a more uniform structure with fragmentation and spheroidization of Si and do not lead to a significant deterioration in hardness. Within the framework of this work, the preferred SA regime was recognized as the 500 °C, 30 min regime due to having a less low temperature, being less time-consuming, and providing the necessary structure (the smallest size and most favorable distribution of Si inclusions without significant grain growth) and properties (the microhardness is at the level of initial properties).
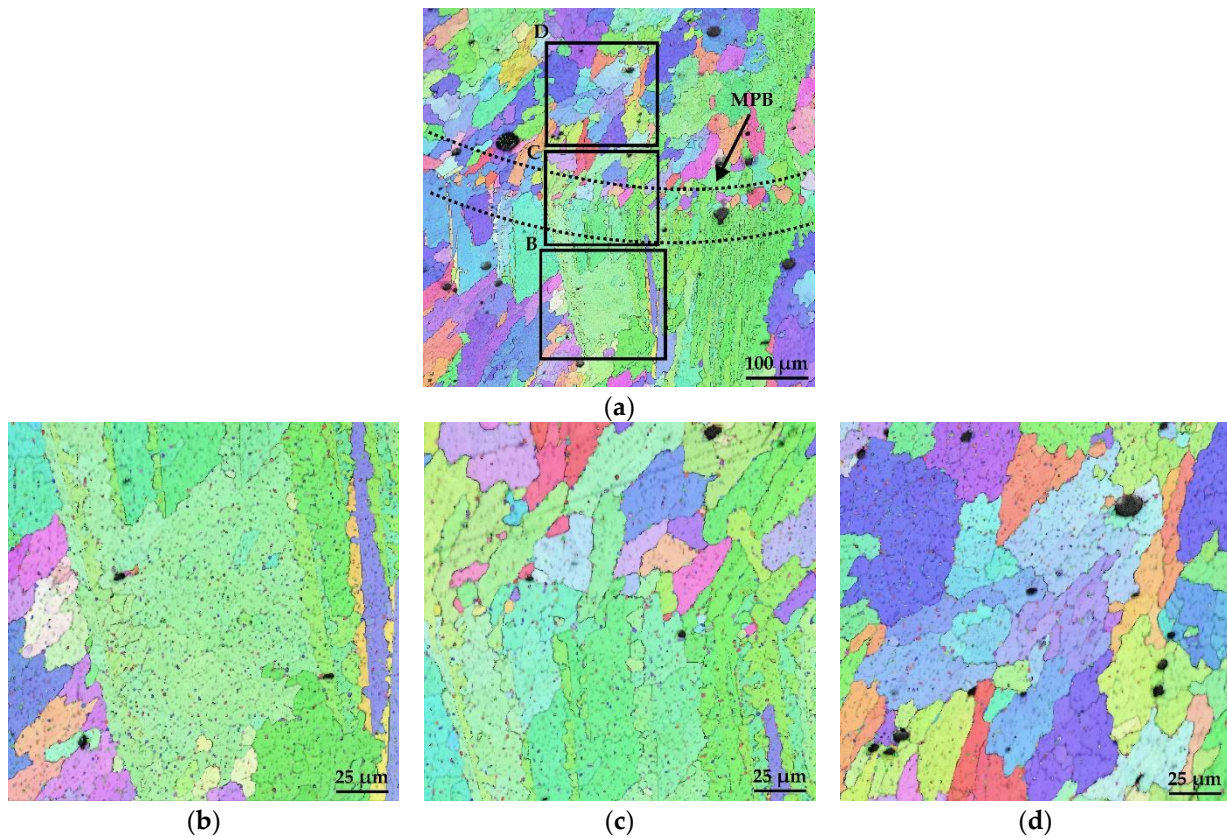
(a)

(b)

(c)

(d)

Figure 15. EBSD analysis results of the SA sample at 500 °C for 30 min ((**a**) overall image; (**b**) enlarged image of section B; (**c**) enlarged image of section C; (**d**) enlarged image of section D).

3.3. Artificial Aging

Preliminary assessment of the quality of AA was conducted by measuring microhardness, the results of which are shown in Figure 16.
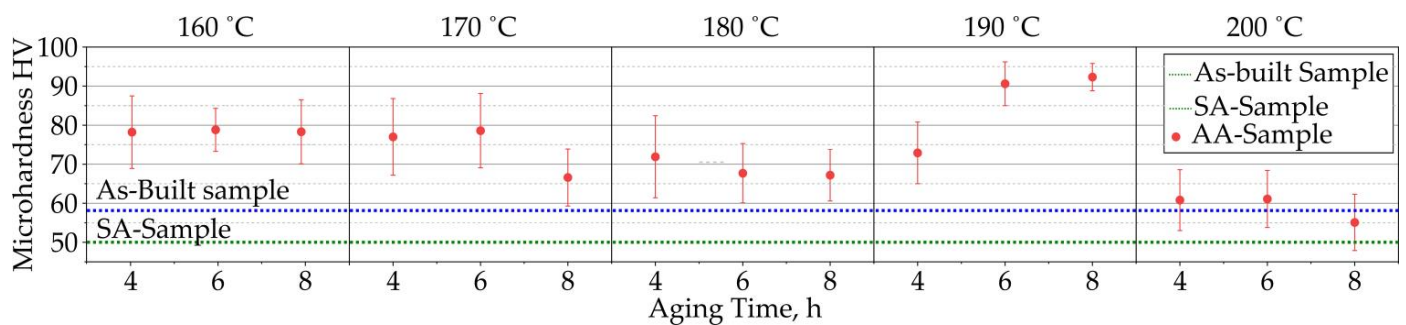

Figure 16. Results of microhardness measurement of AA samples.

From the results of measuring the microhardness of AA samples, it can be seen that at a heat treatment temperature of 160 °C, the effect of holding time on the microhardness value is minimal, and the values obtained at this AA are 78 HV. At a temperature of 170 °C, the effect of holding time on microhardness becomes noticeable: the values obtained after 4 and 6 h of AA give similar microhardness values of 78 HV, while holding for 8 h leads to a decrease in hardness to 66 HV. The maximum microhardness value is achieved at a temperature of 190 °C, with holding times of 6 and 8 h giving similar values of 90–92 HV, which is 55% higher than the value in the initial state and 80% higher than the SA state. Further increasing the thermal treatment temperature to 200 °C leads to a significant

decrease in hardness, which with an increase in holding time to 8 h approaches the SA state.

The likely cause of the increase in microhardness is the formation of nanoscale Mg-Si particles. To verify this assumption, an analysis of the material in the heat-treated state was performed using TEM, the results of which are shown in Figure 17.
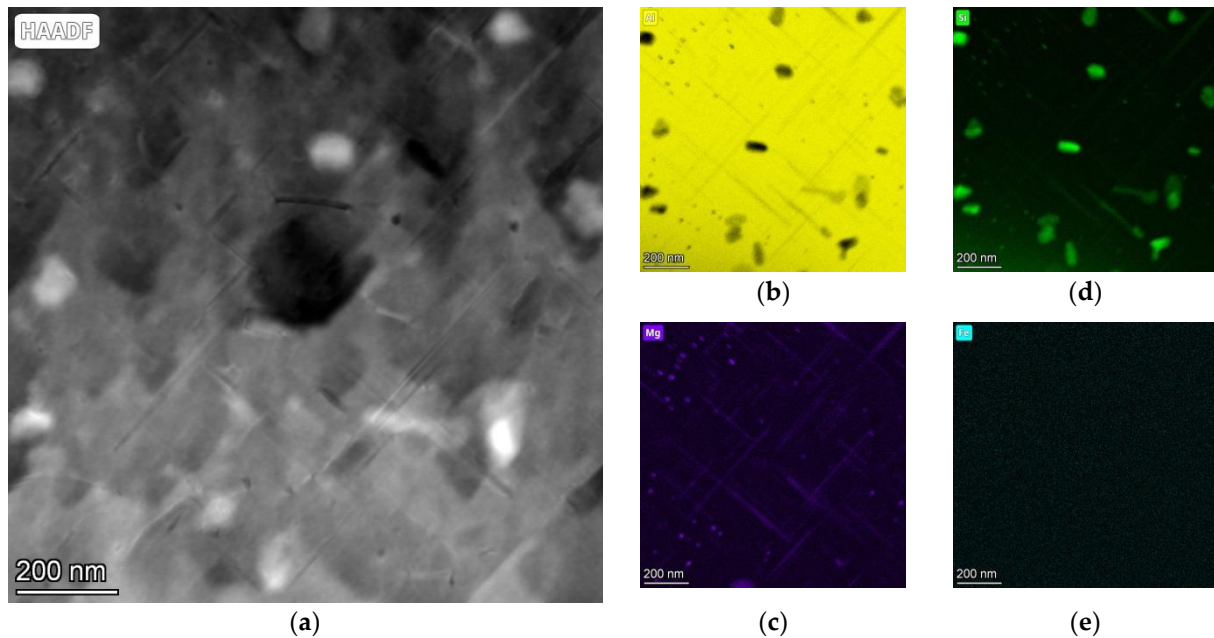

Figure 17. STEM image of the AA sample at 190 °C for 6 h ((**a**) overall image; (**b**) Al distribution map; (**c**) Mg distribution map; (**d**) Si distribution map; (**e**) Fe distribution map).

Using STEM mapping, it was established that, indeed, as a result of AA, nanoscale inclusions enriched in Mg and Si, with a morphology of thin needles about 500 nm long and about 20 nm thick, are precipitated in the α-Al matrix. For a more accurate determination of the phase composition, an HT image with FFT images was taken, the results of which are shown in Figure 18.
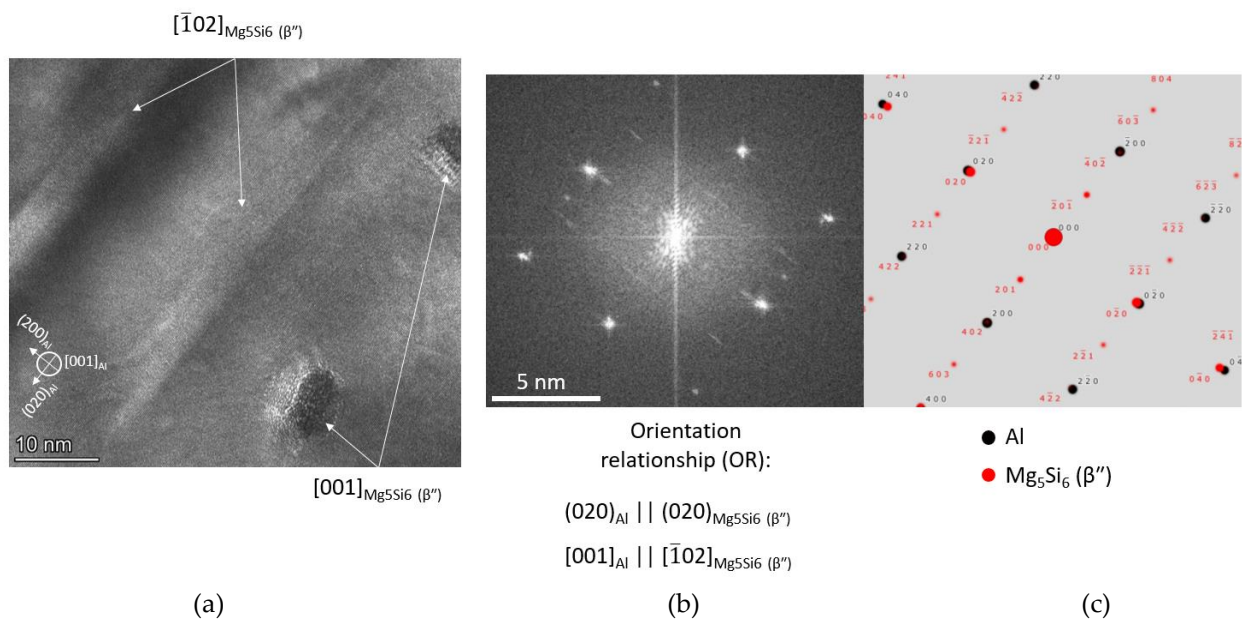

Figure 18. Phase analysis of the sample ((**a**) HR image; (**b**) FFT image; (**c**) FFT image interpretation).

As can be seen from Figure 18, nanoscale inclusions of β'' (Mg_5Si_6) are precipitated in the α-Al matrix. The orientation relationships were $(020)_{Al} || (020)_{Mg5Si6(\beta'')}$ and $[001]_{Al} || [02]_{Mg5Si6(\beta'')}$.

The aging process involves the decomposition of a supersaturated solid solution, initially forming unstable Guinier–Preston (GP) zones enriched with the alloying element, followed by the formation of more stable strengthening phases in subsequent stages, along with their further growth. The authors of [30] proposed the following sequence of precipitation during aging of aluminum alloys: Al SSS $\rightarrow$ aggregation of Si/Mg atoms (GP zones) $\rightarrow$ dissolution of Mg $\rightarrow$ formation of Si/Mg atom cluster $\rightarrow$ a small number of unknown phases $\rightarrow$ precipitation of β'' phase $\rightarrow$ precipitations of β' and β'' phases $\rightarrow$ stable precipitation of β-Mg_2Si. As reported in some works on SLM-AlSi10Mg [31], the formation of stable β-Mg2Si precipitation is observed in the samples as a result of AA heat treatment. Nevertheless, as shown in this work, AA at 190 °C for 6 h in L-DED AlSi10Mg results in the formation of β'' precipitates with the peak microhardness. These phase changes in the alloy are driven by the diffusion of the alloying element within the α-Al matrix. It is known that as the temperature increases, the diffusion of elements accelerates, leading to an earlier achievement of the aged state with the precipitation of strengthening phases and peak hardness compared to lower temperatures. From Figure 15, it is evident that at heat treatment temperatures of 160–180 °C, the hardness of the samples can be increased; however, within the considered time range, the aged state with peak hardness is not achieved, indicating incomplete diffusion [31]. The aging process, with the formation of strengthening phases enriched with Mg and Si, proceeds most completely at a temperature of 190 °C, and peak hardness is achieved after an aging time of 6 h with formation of β'' precipitates, which corresponds with [31]. Further increasing the temperature to 200 °C likely results in Ostwald ripening [18], where larger inclusions grow at the expense of smaller ones, leading to a significant decrease in microhardness.

In this work, the preferred AA regime was chosen to be 190 °C for 6 h, since this AA regime leads to the most complete diffusion, β'' (Mg_5Si_6) formation, and, as a consequence, a 55% increase in hardness compared to the initial state.

4. Conclusions

This study investigated the aluminum alloy AlSi10Mg in the state after L-DED, as well as in the state after solution annealing and artificial aging. The main conclusions are as follows:

- The structure of the alloy in the initial state is a eutectic-type structure, α-Al + Si. The morphology of the eutectic network is non-uniform and changes across the section of the cladded bead. The average grain size at the top of the cladded beads was 60 μm, that at the cladded bead boundaries was 15 μm, and that at the bottom of the cladded beads was 74 μm. The microhardness of the alloy is 58 HV.
- As a result of solution annealing, it was possible to bring the structure to a more uniform state: the developed network of eutectic plates transforms into separate spherical inclusions. The minimum size of such inclusions was achieved with the 500 °C, 30 min regime and is 0.71 μm^2. This regime does not lead to grain growth (the average grain size at the top of the cladded beads was 62 μm, that at the cladded bead boundaries was 15 μm, and that at the bottom of the cladded beads was 85 μm) or to a significant decrease in microhardness (the microhardness was 50 HV).
- As a result of artificial aging, it was possible to achieve a significant increase in microhardness to 90 HV with the 190 °C, 6 h regime. This value is 55% higher than the value in the initial state and 80% higher than the SA state. It has been proven that

the increase in microhardness is associated with the formation of nanoscale inclusions β″ (Mg_5Si_6).

References

1. Patel, S.; Liu, Y.; Siddique, Z.; Ghamarian, I. Metal additive manufacturing: Principles and applications. *J. Manuf. Process.* **2024**, *131*, 1179–1201. [CrossRef]
2. Das, A.; Ghosh, D.; Lau, S.-F.; Srivastava, P.; Ghosh, A.; Ding, C.-F. A critical review of process monitoring for laser-based additive manufacturing. *Adv. Eng. Inform.* **2024**, *62 Pt D*, 102932. [CrossRef]
3. Wu, X.; Yan, H.; Zhou, Y.; Zhang, P.; Lu, Q.; Shi, H. Review of additive manufactured metallic metamaterials: Design, fabrication, property and application. *Opt. Laser Technol.* **2025**, *182 Pt A*, 112066. [CrossRef]
4. Kong, Z.; Wang, X.; Hu, N.; Jin, Y.; Tao, Q.; Xia, W.; Lin, X.-M.; Vasdravellis, G. Mechanical properties of SLM 316 L stainless steel plate before and after exposure to elevated temperature. *Constr. Build. Mater.* **2024**, *444*, 137786. [CrossRef]
5. Zhou, L.; Chen, F.; Cao, S. Effects of longitudinal alternating magnetic field on the microstructure and properties of CMT WAAM Al-5 %Mg alloy. *Mater. Today Commun.* **2024**, *41*, 110272. [CrossRef]
6. Evstifeev, A.; Volosevich, D.; Smirnov, I.; Yakupov, B.; Voropaev, A.; Vitokhin, E.; Klimova-Korsmik, O. Comparative study of the relationship between microstructure and mechanical properties of aluminum alloy 5056 Fabricated by additive manufacturing and rolling techniques. *Materials* **2023**, *16*, 4327. [CrossRef]
7. Shahwaz, M.; Nath, P.; Sen, I. Recent advances in additive manufacturing technologies for Ni-based Inconel superalloys—A comprehensive review. *J. Alloys Compd.* **2024**, 177654. [CrossRef]
8. Srivastava, M.; Jayakumar, V.; Udayan, Y.; Sathishkumar, M.; Muthu, S.M.; Gautam, P.; Nag, A. Additive manufacturing of titanium alloy for aerospace applications: Insights into the process, microstructure, and mechanical properties. *Appl. Mater. Today* **2024**, *41*, 102481. [CrossRef]
9. Li, K.; Yang, T.; Gong, N.; Wu, J.; Wu, X.; Zhang, D.Z.; Murr, L.E. Additive manufacturing of ultra-high strength steels: A review. *J. Alloys Compd.* **2023**, *965*, 171390. [CrossRef]
10. Song, X.; Fu, B.; Chen, X.; Zhang, J.; Liu, T.; Yang, C.; Ye, Y. Effect of internal defects on tensile strength in SLM additively-manufactured aluminum alloys by simulation. *Chin. J. Aeronaut.* **2023**, *36*, 485–497. [CrossRef]
11. Artem, V.I.; Alexandr, M.P.; Elena, M.S.; Tatyana, V.T. Tensile and torsion tests of cylindrical specimens of aluminum alloy ASP35 obtained by the SLM method. *Procedia Struct. Integr.* **2023**, *50*, 113–118. [CrossRef]
12. Cabrera-Correa, L.; González-Rovira, L.; de Dios López-Castro, J.; Botana, F.J. Pitting and intergranular corrosion of Scalmalloy® aluminium alloy additively manufactured by Selective Laser Melting (SLM). *Corros. Sci.* **2022**, *201*, 110273. [CrossRef]
13. Mäkikangas, J.; Rautio, T.; Mustakangas, A.; Mäntyjärvi, K. Laser welding of AlSi$_{10}$Mg aluminium-based alloy produced by Selective Laser Melting (SLM). *Procedia Manuf.* **2019**, *36*, 88–94. [CrossRef]
14. Wang, A.; Wei, Q.; Tang, Z.; Oliveira, J.P.; Leung, C.L.A.; Ren, P.; Zhang, X.; Wu, Y.; Wang, H.; Wang, H. Effects of hatch spacing on pore segregation and mechanical properties during blue laser directed energy deposition of AlSi$_{10}$Mg. *Addit. Manuf.* **2024**, *85*, 104147. [CrossRef]
15. Shi, S.; Lin, X.; Wang, L.; Wang, Z.; Wei, L.; Yang, H.; Tang, Y.; Huang, W. Investigations of the processing–structure–performance relationships of an additively manufactured AlSi$_{10}$Mg alloy via directed energy deposition. *J. Alloys Compd.* **2023**, *944*, 169050. [CrossRef]

16. Yan, Q.; Song, B.; Shi, Y. Comparative study of performance comparison of AlSi$_{10}$Mg alloy prepared by selective laser melting and casting. *J. Mater. Sci. Technol.* **2020**, *41*, 199–208. [CrossRef]

17. Mei, J.; Han, Y.; Sun, J.; Jiang, M.; Zu, G.; Song, X.; Zhu, W.; Ran, X. Improving the comprehensive mechanical property of the AlSi$_{10}$Mg alloy via parameter adaptation of selective laser melting and heat treatment. *J. Alloys Compd.* **2024**, *981*, 173623. [CrossRef]

18. Zheng, Y.; Zhao, Z.; Xiong, R.; Ren, G.; Yao, M.; Liu, W.; Zang, L. Effect of post heat treatment on microstructure, mechanical property and corrosion behavior of AlSi$_{10}$Mg alloy fabricated by selective laser melting. *Prog. Nat. Sci. Mater. Int.* **2024**, *34*, 89–101. [CrossRef]

19. Syrlybayev, D.; Perveen, A.; Talamona, D. Controlling mechanical properties and energy absorption in AlSi$_{10}$Mg lattice structures through solution and aging heat treatments. *Mater. Sci. Eng. A* **2024**, *889*, 145843. [CrossRef]

20. Eremeev, A.D.; Volosevich, D.V. Study of the formation of the structure of laser tracks during laser growing from AlSi$_{10}$Mg alloy powder. *Photonics Russ.* **2021**, *7*, 558–566. [CrossRef]

21. *GOST 23402-78*; Metal Powders. Microscopic Method for Particle Size Determination. Standards Publishers: Moscow, Russia, 1978.

22. *GOST 25849-83*; Metal Powders. Method for Determination of Particle Shape. Standards Publishers: Moscow, Russia, 1983.

23. Di Egidio, G.; Ceschini, L.; Morri, A.; Martini, C.; Merlin, M. A novel T6 rapid heat treatment for AlSi$_{10}$Mg alloy produced by Laser-Based Powder Bed Fusion: Comparison with T5 and conventional T6 heat treatments. *Met. Mater Trans B* **2022**, *53*, 284–303. [CrossRef]

24. *GOST 1497-2023*; Metals. Tensile Test Methods. Standards Publishers: Moscow, Russia, 2023.

25. Mertens, A.; Delahaye, J.; Dedry, O.; Vertruyen, B.; Tchuindjang, J.T.; Habraken, A.M. Microstructure and properties of SLM AlSi$_{10}$Mg: Understanding the influence of the local thermal history. *Procedia Manuf.* **2020**, *47*, 1089–1095. [CrossRef]

26. Zhang, C.; Liao, W.; Shan, Z.; Song, W.; Dong, X. Squeeze casting of 4032 aluminum alloy and the synergetic enhancement of strength and ductility via Al-Ti-Nb-B grain refiner. *Mater. Sci. Eng. A* **2024**, *896*, 146233. [CrossRef]

27. Zhang, C.; Dong, T.; Li, F.; Chen, G.; Guo, Z.; Yuan, D.; Chen, S.; Chen, K. The effect of inhomogeneous microstructures on strength and stress corrosion cracking of 7085 aluminum alloy thick plate. *J. Mater. Res. Technol.* **2024**, *30*, 6163–6175. [CrossRef]

28. Yang, Y.; Chen, J.; Gao, L.; Zhang, T.; Zhang, Z.; Wang, Q.; Zhang, X. Low-cycle fatigue behaviour of extruded 7075 aluminium alloy bar: Competition of grain sizes and textures. *Mater. Sci. Eng. A* **2024**, *897*, 146258. [CrossRef]

29. Tabatabaei, N.; Zarei-Hanzaki, A.; Moshiri, A.; Abedi, H.R. The effect of heat treatment on the room and high temperature mechanical properties of AlSi$_{10}$Mg alloy fabricated by selective laser melting. *J. Mater. Res. Technol.* **2023**, *23*, 6039–6053. [CrossRef]

30. Edwards, G.A.; Stiller, K.; Dunlop, G.L.; Couper, M.J. The precipitation sequence in Al-Mg-Si alloys. *Acta Mater.* **1998**, *46*, 3893–3904. [CrossRef]

31. Wei, P.; Chen, Z.; Zhang, S.; Fang, X.; Lu, B.; Zhang, L.; Wei, Z. Effect of T6 heat treatment on the surface tribological and corrosion properties of AlSi$_{10}$Mg samples produced by selective laser melting. *Mater. Charact.* **2021**, *171*, 110769. [CrossRef]